Metastable Corundum-Type In_2O_3: Phase Stability, Reduction Properties and Catalytic Characterization

Eva-Maria Köck[1#], Michaela Kogler[1#], Matthias Grünbacher[1], Chen Zhuo[1], Ramona Thalinger[1], Daniela Schmidmair[3], Lukas Schlicker[2,4], Aleksander Gurlo[4], Simon Penner[1,*]

[1]Institut für Physikalische Chemie, Universität Innsbruck, Innrain 80-82, A-6020 Innsbruck

[2] Fachbereich für Material-und Geowissenschaften, Technische Universität Darmstadt, Jovanka-Bontschits-Straße 2, D-64287 Darmstadt

[3]Institut für Mineralogie und Petrographie, Universität Innsbruck, Innrain 52d, A-6020 Innsbruck

[4] Fachbereich Keramische Werkstoffe/Chair of Advanced Ceramic Materials, Institut für Werkstoffwissenschaften- und technologien, Technische Universität Berlin, Hardenbergstraße 40, D-10623 Berlin

# These two authors contributed equally to this work.

Corresponding Author: S. Penner, simon.penner@uibk.ac.at, Tel: 0043 512 507 58003

Abstract

The phase stability, reduction and catalytic properties of corundum-type rhombohedral In_2O_3 have been comparatively studied with respect to its thermodynamically more stable cubic In_2O_3 counterpart. Phase stability and transformation were observed to be strongly dependent on the gas environment and the reduction potential of the gas phase. As such, reduction in hydrogen caused both the efficient transformation into the cubic polymorph as well as the formation of metallic In especially at high reduction temperatures between 573 K and 673 K. In contrast, reduction in CO suppresses the transformation into cubic In_2O_3, but leads to a larger quantity of In metal at comparable reduction temperatures. This difference is also directly reflected in temperature-dependent conductivity measurements. Catalytic characterization of rh-In_2O_3 reveals activity in both routes of the water-gas shift equilibrium, which gives rise to a diminished CO_2-selectivity of ~ 60% in methanol steam reforming. This is in strong contrast to its cubic counterpart, where CO_2 selectivities of close to 100 %, due to the suppressed inverse water-gas shift reaction, have been obtained. Most importantly, rh-In_2O_3 in fact is structurally stable during catalytic characterization and no unwanted phase transformations are triggered. Thus, the results directly reveal the application-relevant physico-chemical properties of rh-In_2O_3 which might encourage subsequent studies on other less-common In_2O_3 polymorphs.

1. Introduction

The understanding of the polymorphism of In_2O_3 has evoked recent interest both due to fundamental scientific[1-6] and technological aspects[7-16]. As for the latter, promising use in solar cells, as UV lasers sensors or for catalytic applications has been reported[7-17]. Interest from a basic scientific viewpoint is mainly fuelled by both novel synthesis routes to metastable In_2O_3 modifications and morphologies and understanding of the phase transitions between them[1-4,17,18]. The In_2O_3 phase diagram thereby is currently comprised of five polymorphs, namely cubic bixbyite-type In_2O_3 (thermodynamically stable under ambient conditions), rhombohedral corundum-type rh-In_2O_3 and three orthorhombic modifications, i.e. Rh_2O_3 (II), (III)- and α-Gd_2S_3-type[4,5,19-22]. While rh-In_2O_3 is accessible at ambient pressure, the orthorhombic polymorphs can only be synthesized via dedicated high pressure and high-temperature treatments and usually undergo partial phase transitions upon decompression[4,18-22]. Therefore, physico-chemical characterization is severly hampered and consequently very limited. A recent exception, however, represents the rhombohedral polymorph. Due to the existing and envisioned applications of In_2O_3 as e.g. promising gas sensor and recent advances in morphological control of nanosized oxide particles and crystals, much effort has been placed in obtaining large quantities of rh-In_2O_3 exposing different crystal facets by dedicated and simplified synthesis procedures[1,3,17,23]. Despite this progress, severe limitations still prevail due to the inherent instability also of the rhombohedral modification towards phase transition to the thermodynamically stable cubic phase. The stability range is extremely dependent on a variety of experimental parameters, including gas phase environment and annealing temperature[3]. This limits the available time period to between 30 minutes at 650 °C to hours and days at temperatures between room temperature and 350 °C[24]. Therefore, not much is known about the intrinsic physico-chemical properties of the rhomboehedral polymorph, except limited spectroscopic information (FT-IR and Raman[17]), as well as

structural characterization of dedicated morphologies and theoretical calculations of the electronic structure [1,3,17,23,25,26]. Its properties, nevertheless, play a keyrole in the understanding and further directed knowledge-based synthesis and research. The studies are also partially fuelled by the outstanding reduction behavior and catalytic properties of its cubic counterpart[8,9], which readily loses oxygen upon treatment with various reducing gases (especially hydrogen and carbon monoxide) and therefore gives rise to exceptional properties in the water-gas shift reaction and a very pronounced CO_2-selectivity in the methanol steam reforming reaction[8,9,27].

Thus, the transfer of the experiments to the corresponding rhombohedral phase is most rewarding with respect to elucidating the common properties and differences of the two In_2O_3 modifications. In due course, a rhombohedral sample synthesized via a dedicated non-aqueous solvothermal route will be subjected to identical treatment as its cubic counterpart and studied by an array of spectroscopic (FT-IR spectroscopy, electrochemical impedance spectroscopy, EIS), structural (X-ray diffraction, XRD) and catalytic techniques (water-gas shift reaction, WGSR, and methanol steam reforming, MSR). Applying this pool of methods will, thus, reveal its intrinsic properties and especially also the influence of the eventual phase transition on the physico-chemical properties.

2. Experimental

2.1. Synthesis of the materials

Corundum-type rh-In_2O_3 was obtained by the calcination of metastable indium oxyhydroxide (InOOH) for 30 min at 673 K in ambient air. Phase-pure InOOH was synthesized by a solvothermal route, as described in[24]. The synthesis route allows for the reproducible synthesis of about 3500 mg phase-pure InOOH per synthesis run. The as-synthesized

nanocrystalline rh-In_2O_3 sample has a BET specific surface area of 43.5 m^2 g^{-1}. The reference sample is a cubic In_2O_3 material from Alfa Aesar (99.99%) with a BET specific surface area of ~ 0.74 m^2 g^{-1}, measured on a Quantachrome Nova 2000 Surface and Pore Size Analyzer. To highlight the different structural features directly, Figure S1 provides a comparison of c-In_2O_3 and rh- In_2O_3.

High-purity gases used in the following experiments were provided by Messer-Griesheim. Remaining condensable impurities were further removed by cooling traps set to various temperatures as required by the respective boiling and sublimation points of each gas for the volumetric, impedance and FT-IR experiments. For helium and hydrogen, liquid N_2 at 77 K is used. Oxygen and carbon monoxide were purified by ethanol/liquid N_2 mixtures held at 153 K, CO_2 at 223 K.

2.2. Electrochemical Impedance Spectroscopy (EIS)

A heatable *operando* impedance cell designed for gas treatments up to 1273 K, situated in a tubular furnace (Linn) and controlled by a thermocouple located 5 mm downstream of the sample, together with a Micromega PID temperature controller was used for analysis. Temperature-dependent conductivity (i.e. impedance) measurements were carried out using a IM6e impedance spectrometer (Zahner Elektrik). For all measurements, an excitation frequency of 1 Hz and a stimulation voltage of 20 mV were applied to two circular Pt electrodes (diameter 5 mm) in mechanically enforced contact with the sample (corresponding to a force of 2 N). The latter is a pelletized powder material (several hundred milligrams of the powder are pressed by 2 t into a disk of about 5 mm diameter and about 3-4 mm thickness). Gas treatments are exclusively carried out under flowing conditions (~ 1 mL s^{-1}) up to various temperatures, but not higher than 673 K to eventually avoid triggering phase transformations to a large amount.

2.3. Volumetric Adsorption

All volumetric measurements are carried out in a dedicated quartz glass apparatus, capable of measuring in static or flowing gas mode. Hence, it is used both for temperature-programmed reduction and oxidation experiments under defined static gas conditions and temperature-programmed desorption measurements under flowing conditions. The pressure inside the chamber is measured by a Baratron capacitance manometer (MKS) and the gas flow controlled by mass flow controllers. The powderous samples (several hundred milligrams) are fixed by quartz wool inside the vertical quartz glass tube. Detection of the reactants and reaction products is performed by using a quadrupole mass spectrometer (Balzers) attached to the tube via a capillary leak. For quantification of CO, CO_2 fragmentation is taken into account. Temperature-programmed reduction experiments in either pure hydrogen or carbon monoxide are carried out using defined starting pressures of about 100 mbar. Subsequently, the temperature is ramped standardized with 10 K min^{-1} up to 673 K, followed by a 10 minute isothermal period and re-cooling the sample in the respective gas mixture back to room temperature. The same procedure is applied for temperature-programmed re-oxidation treatments, necessary for quantification of the oxygen defects introduced by the reduction pre-treatment. These dedicated reduction treatments are usually carried out via exposing the sample to flowing hydrogen at various temperatures (~ 1 mL s^{-1}, highest temperature 618 K), re-cooling it to room temperature and subsequently pumping down the reactor to a base pressure of ~ 1.0×10^{-7} mbar. Afterwards, the so-treated sample is heated *in vacuo* with 10 K min^{-1} up to 823 K to remove adsorbed hydrogen and thus, obtaining information on the bonding strength of hydrogen on different surface sites. Similar thermal desorption treatments are also performed after the respective temperature-programmed reduction treatments.

2.4. Catalytic measurements

All experiments were performed in a Labview-controlled re-circulating batch reactor of about 13 mL volume[28]. Reactants are detected by a quadrupole mass analyzer attached to the reactor via a capillary leak. The mass-to-charge ratios (m/z) 2 (hydrogen), 15 and 16 (methane), 28 (carbon monoxide), 29 (formaldehyde/methanol fragment), 30 (formaldehyde), 31 (methanol), 40 (argon) and 44 (carbon dioxide) are routinely collected. Fragmentation patterns for carbon dioxide and methanol are considered and the signal intensities converted to partial pressures via external calibration standards. For a typical (inverse) water-gas shift reaction, about 25 mbar CO and 25 mbar water (about 30 mbar CO_2 and 30 mbar H_2) are used. Methanol steam reforming experiments are carried out using ~ 15 mbar methanol and 30 mbar water. To all reaction mixtures, 10 mbar Ar was added to correct for the permanent gas withdrawal through the leak and He added to 1 bar total pressure for temperature equilibration within the reactor and circumvent heat transfer limitations.

2.5. FT-Infrared Spectroscopy (FT-IR)

All FT-IR spectra were recorded with an Agilent Cary 600 and a home-built high-temperature, high-pressure *operando* quartz reactor cell, capable of collecting spectra at temperatures up to 1300 K and pressures up to 1 bar in reactive gases. Its dedicated construction allows the use of ultra-dry conditions with a water partial pressure below 1.0×10^{-7} mbar[29]. For analysis, the powders (~ 20 mg) are pressed into thin pellets using a hydraulic press at ~ 1-2 t. Treatments under flowing and static conditions are possible.

2.6. X-ray diffraction (XRD)

Two types of X-ray diffractometers are used for analysis. Samples treated via the volumetric and catalytic experiments are analyzed with a Siemens D5000 under ambient conditions using Cu-K_α radiation (1.54178 Å) at 300 K in the 2θ range 10 to 70° with a step size of 0.02° in

Bragg-Brentano geometry. Due to the low sample amount, X-ray diffractograms of samples after EIS treatments were collected with a Bruker AXS D8-Advance powder diffractometer also in Bragg-Brentano geometry. The samples were prepared on a rotatable Si single crystal to minimize background signals. The range of measurement was chosen from 2θ = 20 to 90° with a step size of 0.02°.

3. Results and Discussion

3.1. Phase stability and reducibility

Hydrogen on rh-In_2O_3

Hydrogen interaction and adsorption is at first measured in the respective temperature-programmed hydrogen reduction experiments as provided in Figure 1. Considerable uptake only sets in above ~ 530 K with a single consumption step up to the highest temperatures of 673 K. In the following isothermal period, further hydrogen uptake points towards still prevailing kinetic limitations. Upon re-cooling to room temperature, the hydrogen remains adsorbed on the surface. Comparing this to c-In_2O_3, the overall features are comparable[27], but distinct differences are: (i) the uptake process on rh-In_2O_3 does not proceed via clearly distinguishable steps and (ii) the main consumption occurs only at and above ~570 K, in contrast to c-In_2O_3, where this uptake starts at ~500 K. A slight hydrogen uptake is, nevertheless, visible starting at ~300 K, followed by a plateau region before the uptake drastically increases. This is in fact similar to c-In_2O_3, where it has been assigned to surface-restricted reduction[27]. The total surface-normalized consumed amount is also comparable at around 10 µmol m^{-2}. A subsequent thermal desorption spectrum after re-cooling to room temperature (inset in Figure 1) reveals three discernible desorption steps at 540, 650 and 750 K, indicating at least three energetically different binding sites for hydrogen. This again reveals direct differences to c-In_2O_3, which when treated under similar conditions reveals only

two prominent peaks (at 550 and 800 K)[27]. Note that the X-ray diffractogram taken after performing the TPD after TPR (cf. Figure 3, pink trace), cubic In_2O_3 appears in the pattern, which might explain the peak at 550 K, but the other two are clearly associated with rh-In_2O_3.

Further information is given by additional temperature-programmed hydrogen desorption experiments. These are exclusively conducted under flowing hydrogen conditions and subsequent hydrogen desorption (cf. Experimental section). Note already at this stage the different conditions with respect to the previously discussed temperature-programmed reduction experiments, which are conducted in a static hydrogen atmosphere. The main difference, hence, is the presence or removal of reactant water, formed by eventual release of oxygen from the lattice, resulting in an oxygen vacancy and gas-phase water.

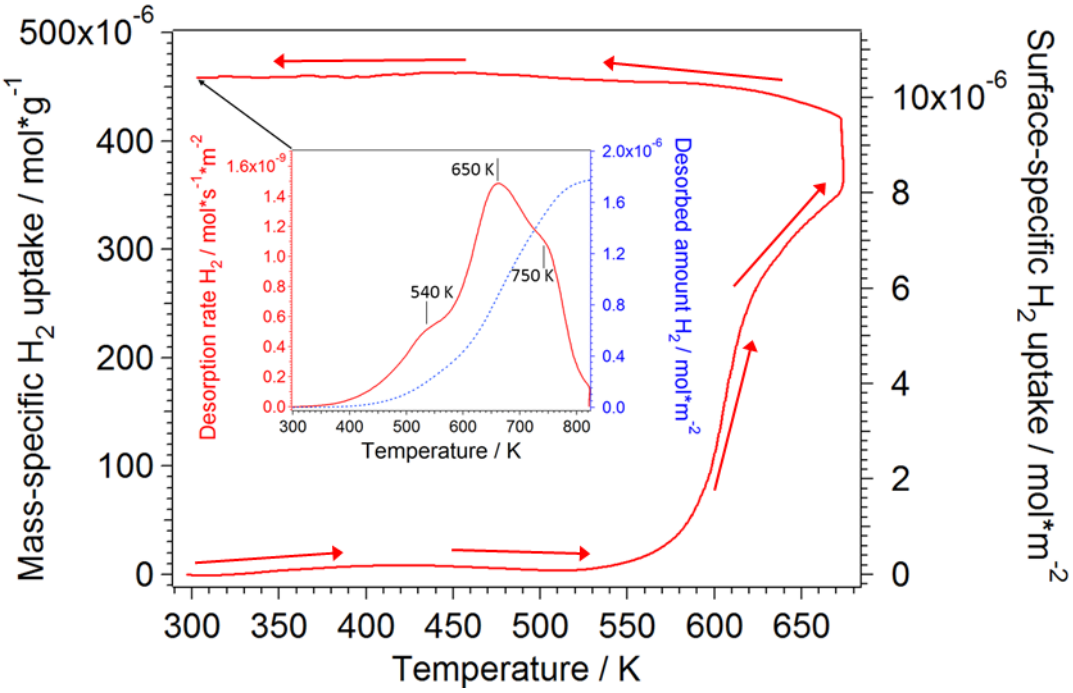

Figure 1: Temperature-programmed hydrogen uptake measurement (main panel) and subsequent thermal desorption after re-cooling to room temperature (red) alongside the total desorbed amount of hydrogen (blue), shown as inset. Initial starting pressure of hydrogen: 100 mbar, heating and cooling rate: 10 K min^{-1}, isothermal period: 10 minutes at 673 K. The direction of the arrows indicates the heating-cooling cycle.

Figure 2 in turn highlights these experiments at three selected reduction temperatures up to ~ 620 K. The maximum TPD temperature has been restricted to 720 K to prevent a considerable transformation into cubic In_2O_3. After reduction at 553 K and 567 K, a TPD similar to the one obtained after the temperature-programmed reduction is obtained, with two prominent desorption peaks at 600 K and 640 K, and less pronounced shoulders at 520 K, 660 K and ~ 700 K, respectively. Whereas the low-temperature shoulder appears fixed, the maximum of the most prominent peak shifts to lower temperatures with increasing reduction temperature. Consistently, the amount of surface-normalized consumed hydrogen rises from 1.4 to 2.2 µmol m^{-2}. The situation is slightly more complex at even higher reduction temperatures of 618 K. One very pronounced peak at ~ 690 K is visible, with a shoulder at ~ 640 K. Most interesting, the total adsorbed hydrogen amount slightly decreases to 2.0 µmol m^{-2} as compared to reduction at 567 K. This appears contradicting at first, but can be related to two helpful observations: (i) the desorbed amount of water is highest after reduction at 618 K (cf. inset in Figure 2; adsorbed hydrogen can be released basically in two competing ways – either by desorption as H_2 or as reactant water by removal of oxygen from the lattice) and (ii) as it follows from the X-ray diffractograms highlighted in Figure 3, reduction at and above 573 K in principle causes partial transformation into the c-In_2O_3 polymorph and at the highest temperatures, also metallic In. Substantial influence of the former (despite being present in the X-ray diffractograms after reduction at 473 and 573 K in amounts of ~ 10-12 weight-%, according to Rietveld analysis, see Figure 3 and Table 1) can be excluded, as the hydrogen desorption peaks of c-In_2O_3 are observed at different temperatures[27]. Formation of metallic In is not observed up to reduction temperatures of ~600 K, but above, especially at 673 K, 10 weight-% In metal and 90 weight-% c-In_2O_3 are present, while no rh-In_2O_3 is left at all after treatment at the highest reduction temperatures. This, obviously, has to be taken into account when discussing the TPD spectrum obtained after reduction at 618 K in detail, blurring

potential trends in total hydrogen uptake and peak shifts. Similar decreased hydrogen adsorption capabilities after formation of metallic In have also been observed on c-In_2O_3.[27]

To clarify the stability and the eventually introduced c-In_2O_3 phase and possibly also metallic In, X-ray diffractograms have been recorded after each reduction step and the resulting crystalline phases quantified by Rietveld analysis. Figure 3 and Table 1 summarize these experiments. In fact, rh-In_2O_3 is perfectly stable after performing the static temperature-programmed reduction in hydrogen up to 673 K and even after treating the sample in flowing hydrogen at 473 K (i.e. the TPD experiment at the lowest temperatures). At higher temperatures in flowing hydrogen, slight amounts of c-In_2O_3 are formed (573 K) and at even higher temperatures (673 K), full transformation into c-In_2O_3, as well as further reduction to metallic In, takes place. After the TPD performed subsequent to the TPR experiment, a substantial amount of c-In_2O_3 is observed, but no metallic In. A comparison to c-In_2O_3 reveals that the transformation into metallic In is significantly suppressed on rh-In_2O_3 in comparison to c-In_2O_3. Whereas on the latter clear signals of presence of metallic In are already observed after reduction at ~ 600 K, this is not the case for the polymorph presented here. This certainly rises questions about the influence of the polymorph intertransition on the reduction. Thus, the presented results offer the most probable explanation in terms of a subsequent transformation of rh- into c-In_2O_3, which is then followed by easier reduction of the latter into metallic In. The critical temperature region obviously is the one between 573 and 673 K.

Furthermore, the presented TPD results also allow to estimate the number of oxygen vacancies formed during reduction. The estimation is based on controlled re-oxidation in a defined oxygen partial pressure (~ 200 mbar initial oxygen pressure, heating ramp 10 K min^{-1}). As expected, for the lowest reduction temperatures, the number of introduced oxygen vacancies is smallest and seemingly does not change up to a reduction temperature of 573 K (cf. Table 2). Above, the O_2 consumption increases drastically, indicating that the threshold

temperature for efficient oxygen vacancy formation is found at around 573 K (cf. drastic hydrogen uptake in Figure 1). Together with the data in Figure 2, we might infer at least two different temperature-dependent pathways of hydrogen interaction: hydrogen adsorption at lower reduction temperatures (finally desorbing as hydrogen molecule during TPD) and oxygen vacancy formation (forming reactant water during reduction) at temperatures above 573 K.

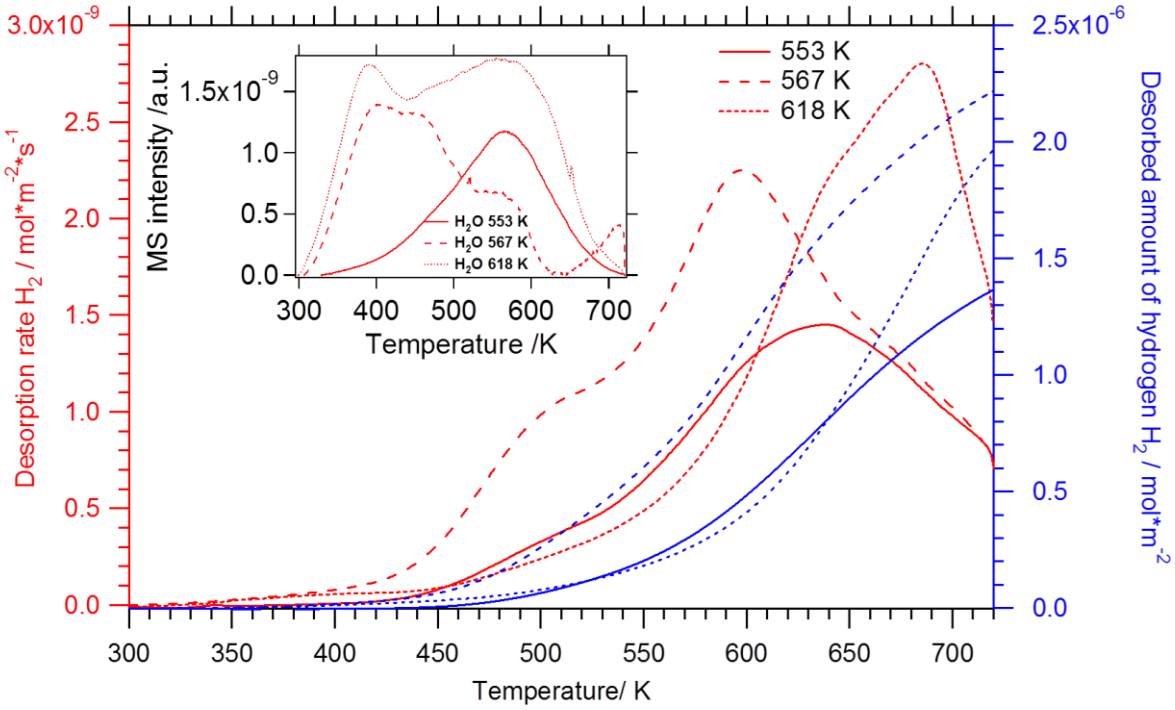

Figure 2: Thermal desorption spectra of hydrogen (main panel) and water (inset) after treatment of rh-In_2O_3 in flowing hydrogen (1 h, 1 mL s^{-1}) at different reduction temperatures. Heating rate: 10 K min^{-1}. Desorption rate shown in red, total desorbed amount of hydrogen in blue.

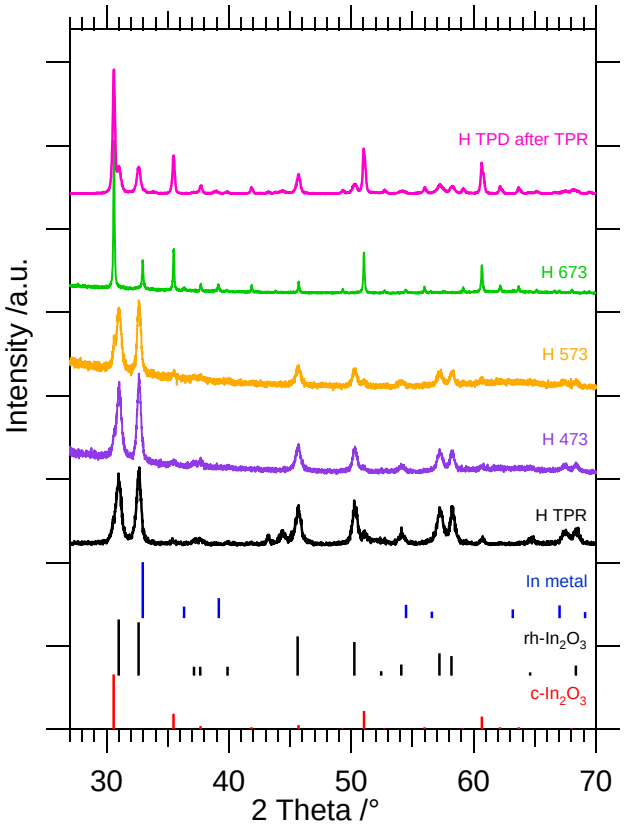

Figure 3: X-ray diffractograms collected after various flowing and static treatments in hydrogen as indicated. Color code: purple, orange and green denote flowing treatments (1 h, 1 mL s^{-1}) at 473, 573 and 673 K, respectively. Black represents the pattern after the TPR experiments and pink after the subsequent TPD. The calculated peak assignment of the rh-In_2O_3 (black), c-In_2O_3 (red) and In metal (blue) phases is based on PDF cards 22-0336, 06-0416 and 05-0642 (ICDD Powder Diffraction database 4+) and given as solid bars at the bottom of the graph.

Table 1: Rietveld analysis after selected reduction treatments on rh-In_2O_3. Weight-% are rounded to 5 weight-%.

Sample and Treament/ K	**rh-In_2O_3/ weight-%**	**c-In_2O_3/ weight-%**	**metallic In/ weight-%**
H-473	90	10	-

H-573	85	15	-
H-673	-	90	10
CO-523	90	10	-
CO-673	40	30	30
CO-CO_2-673	25	70	5
CO-H_2O-673	80	20	-

Table 2: Quantification of the temperature-programmed re-oxidation treatment as an estimate of the formed oxygen vacancies during flowing reduction in hydrogen.

Sample and Treament/ K	**O_2 consumption/ µmol g^{-1}**	**O_2 consumption/ µmol m^{-2}**
H-414	5.9	0.13
H-553	4.6	0.10
H-567	8.1	0.18
H-618	85	1.94

The influence of the reduction on the material's properties of rh-In_2O_3 is further highlighted by temperature-programmed impedance, i.e. conductivity measurements. Previous experiments on the c-In_2O_3 polymorph already indicated the valuable information especially with respect to the formation of metallic In during the reduction process[27]. Figure 4 shows comparative impedance traces in dry hydrogen in comparison to treatment in CO. While the latter will be discussed in detail in the following section, even the comparative discussion of the behavior in hydrogen reveals interesting features. In contrast to c-In_2O_3, which showed a rapid decrease of the impedance in one single step down to metallic conductivity at around 400 K,[27] the corresponding trace on rh-In_2O_3 is significantly different. A continuous decrease of the impedance is observed, starting at around 300 K. At 500 K, where on c-In_2O_3 metallic conductivity is already reached, a distinct temperature-independent plateau in the conductivity of about 50 K range is entered. At higher temperatures, yet another impedance drop finally leads to metallic conductivity, which is preserved up to 673 K and also upon re-cooling to room temperature. Rietveld analysis (important points have been marked in Figure 4) shows

that the plateau is not connected to the formation of metallic In, but must be associated with small structural changes (especially the transformation from rh-In_2O_3 into c-In_2O_3), as from 473 K to 573 K, only 5 weight-% of rh-In_2O_3 are converted into c-In_2O_3. Most interesting, but in accordance with associated experiments on c-In_2O_3,[27] metallic conductivity is reached even before metallic In shows up in the X-ray patterns. Relating the conductivity experiments to thermal hydrogen desorption experiments and oxygen vacancy formation, it turns out that up to 573 K (where finally metallic conductivity is reached) oxygen vacancy formation is not a dominant issue. Only at higher temperatures, when the vacancy concentration rises drastically, substantial formation of metallic In takes place and the impedance drops to metallic behavior (low Ω-range). Vice versa, below reduction temperatures of 573 K, the impedance must be associated with adsorbed hydrogen (and water giving rise to a more or less hydroxylated surface) and is therefore most likely a strictly surface-bound conduction phenomenon.

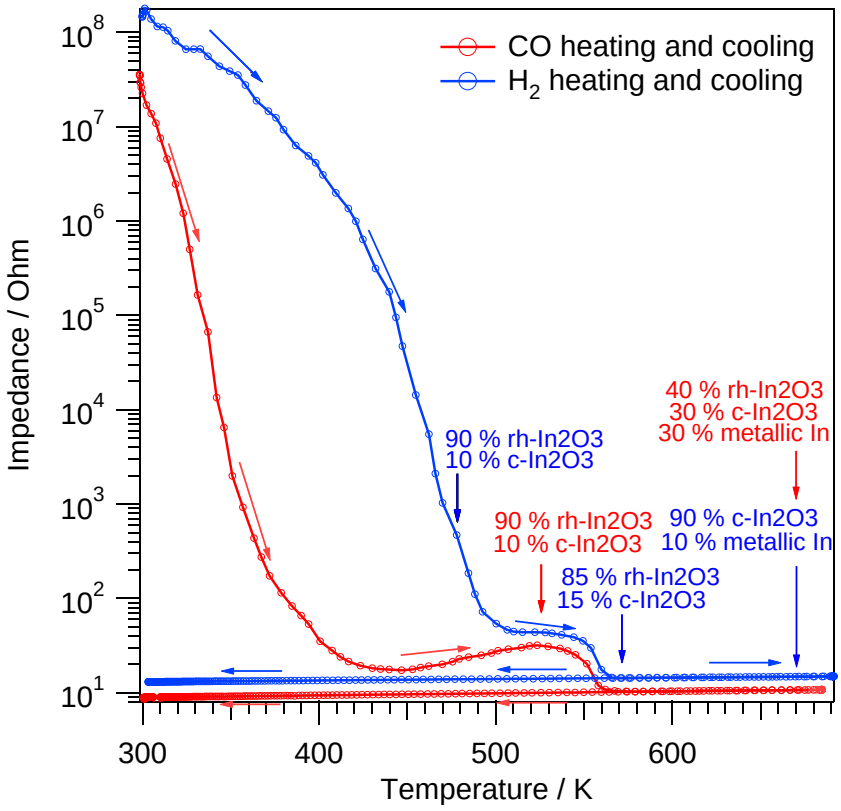

Figure 4: Temperature-programmed *in situ* electrochemical impedance measurements in dry hydrogen (blue) and CO (red). The temperature is ramped from 300 K to 673 K and back, including an isothermal period at 673 K for 10 minutes. Ramp: 10 K min^{-1}. Phase analysis according to Rietveld analysis from the associated X-ray diffractograms at important points has been marked. The direction of the arrows indicates the heating-cooling cycle.

Carbon Monoxide on rh-In_2O_3

In direct comparison to the reduction experiments in hydrogen, the temperature-programmed reduction experiments in CO (Figure 5A) reveal conversion into CO_2, most probably by removal of and reaction with lattice oxygen, starting efficiently at ~550 K and proceeding also during the 10-minute isothermal period. Upon re-cooling, a small amount is re-formed, also indicated by the respective CO_2 consumption in the same temperature region. The same is also directly visible in the corresponding FT-IR experiments (Figure 5B). Above 573 K, CO_2 appears in the gas phase, in close correlation to the decrease in the CO signal around 550 K in the temperature-programmed reduction experiment.

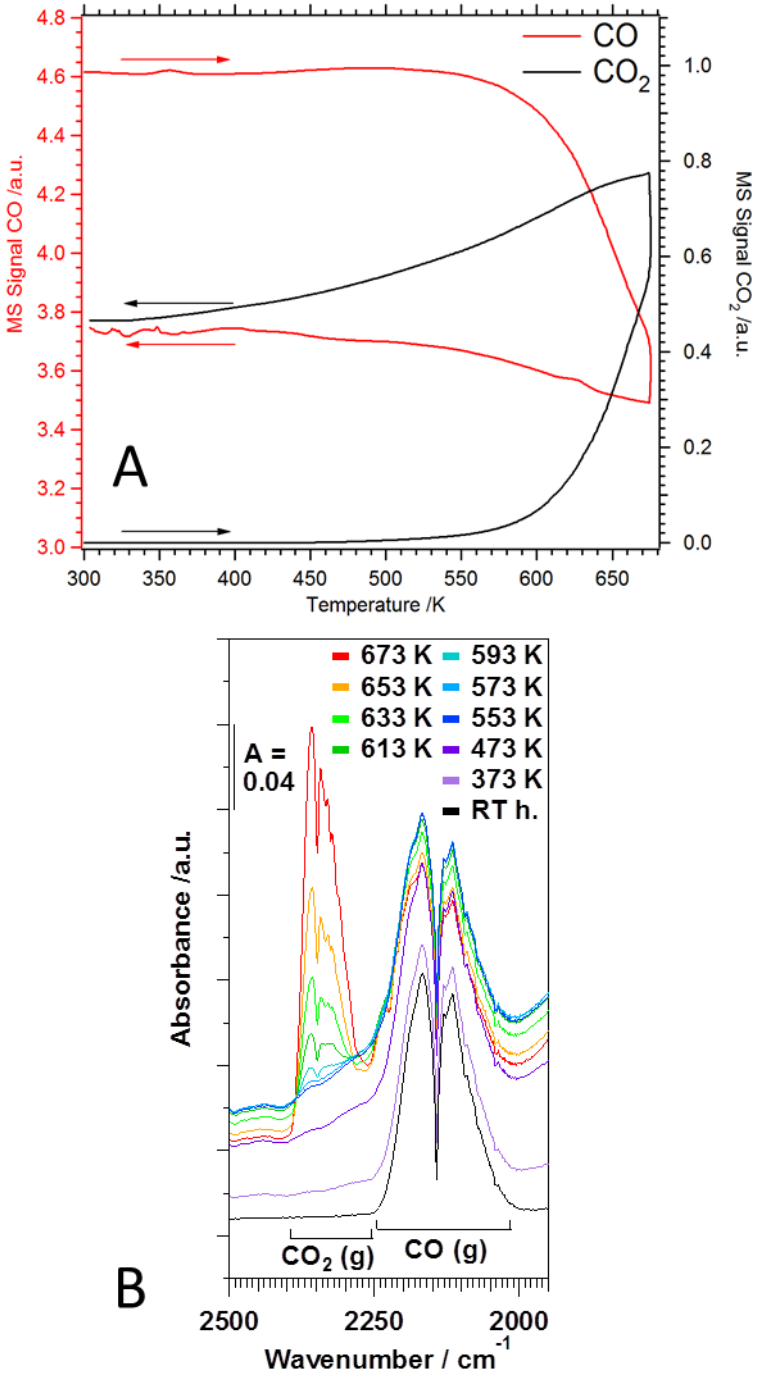

Figure 5: Panel A: Temperature-programmed carbon monoxide uptake. Initial starting pressure of carbon monoxide: 100 mbar, heating and cooling rate: 10 K min^{-1}, isothermal period at 673 K for 10 minutes. The direction of the arrows indicates the heating-cooling cycle. Panel B: Static temperature-programmed CO FT-IR experiments in direct comparison to the temperature-programmed reduction experiment shown in Figure 6A. Starting CO pressure: 121 mbar, heating and cooling rate: 10 K min^{-1}.

Also the corresponding temperature-dependent conduction behavior as a direct consequence of the different reduction behavior in CO and hydrogen yields valuable information. Re-addressing Figure 4, decrease of the impedance is already observed starting at room temperature until at 420 K a quasi temperature-independent impedance plateau (~ 20 Ω) is reached. This plateau extends up to ~ 550 K, above which a further drop leads to metallic conductivity. The drop, most interestingly, occurs at almost exactly the same temperature as in hydrogen (also the amount of c-In_2O_3 formed via treatment in H_2 and CO is comparable at lower temperatures), but the distribution between c-In_2O_3, rh-In_2O_3 and metallic In at higher temperatures (above 573 K) is clearly different. In fact, the transformation into c-In_2O_3 using CO as reducing agent is effectively suppressed (40 weight-% rh-In_2O_3 still remaining at 673 K, as compared to 0 weight-% on c-In_2O_3), but at the same time, the amount of metallic In at the same temperature (i.e. 673 K) is three times as large (cf. Figure 4 and 6). This indicates that CO obviously strongly affects the reduction to metallic In, but it appears that this is at least not directly correlated to the intertransformation of the In_2O_3 polymorphs. Further, the X-ray diffractograms in Figure 6 once again corroborate the importance of efficient control of the gas phase chemical reduction potential. While the above discussed mixture of both oxide polymorphs and metallic In is obtained after the flowing CO treatment up to 673 K, after the CO TPR shown in Figure 6, the X-ray diffractogram is essentially unchanged and the phase transformation into c-In_2O_3 is triggered only to a very small extent. Table 1 also reveals that adding CO_2 or H_2O has a huge influence on the transformation behavior. Adding CO_2 (1:1 mixture) to CO suppresses the significant formation of metallic In at 673 K, but encourages the transformation to c-In_2O_3. In contrast, adding H_2O (also a 1:1 mixture), suppresses both transformation into either c-In_2O_3 or metallic In. As both additives have a considerable impact on the defect chemistry on rh-In_2O_3 (and the catalytic behavior in the water-gas shift equilibrium, as shown in section 3.2.), we might assume a partial replenishment of the defects in both CO_2 or H_2O, effectively stabilizing rh-In_2O_3.

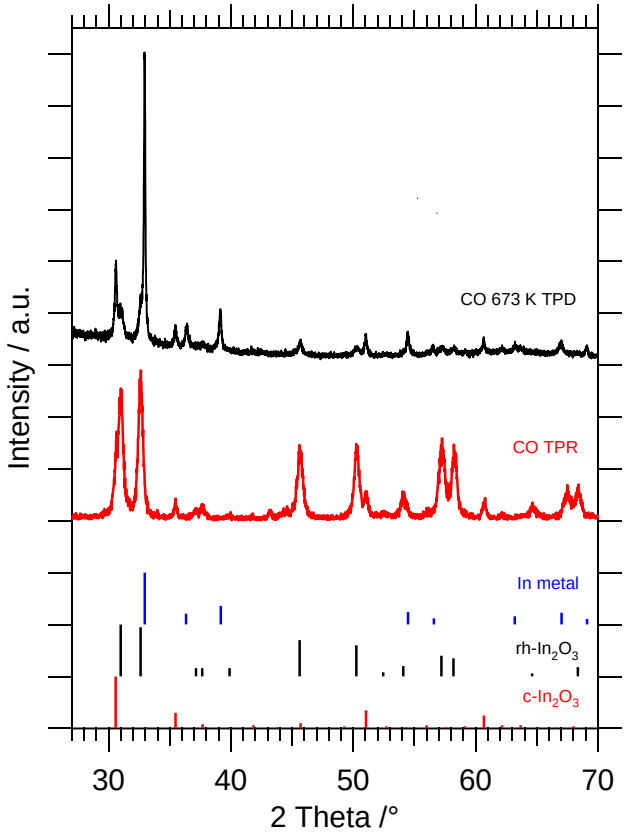

Figure 6: X-ray diffractograms collected after various flowing and static treatments in carbon monoxide as indicated. Black represents the pattern after the TPR experiments and red after a flowing treatment in dry CO at 673 K. The calculated peak assignment of the rh-In_2O_3 (black), c-In_2O_3 (red) and In metal (blue) phase is based on PDF cards 22-0336, 06-0416 and 05-0642 (ICDD Powder Diffraction database 4+) and given as solid bars at the bottom of the graph.

3.2. Catalytic Characterization

(Inverse) water-gas shift reactivity

Together with the MSR reaction profiles, the reactivity in the (inverse) water-gas shift equilibrium is considered to shed most light on the different surface chemistry of the different polymorphs and to eventually explain a different CO_2 selectivity in MSR. Figure 7 A and 7 B show the inverse water-gas shift and water-gas shift reactivity, respectively. The inverse

reaction (Panel A) is characterized by a drop in the CO_2 signal at 630 K with simultaneous increase of CO. Hydrogen is consumed, too, but the consumption starts already at around 470 K, well before the inverse water-gas shift reaction sets in. Above 600-630 K, a further drop in the hydrogen signal indicates the beginning of the stoichiometric inverse water-gas shift reaction. This behavior can be satisfactorily explained by the temperature-programmed reduction and desorption experiments discussed in detail in section 3.1., which showed that hydrogen adsorption (and oxygen vacancy formation) exactly starts in this temperature region, obscuring the inverse water-gas shift reactivity. The water-gas shift direction (Panel B) shows a slightly complexer behavior. Consumption of CO and subsequent formation of CO_2 (starting at around 500 K) is expected based on the results of section 3.1., but a simple oxygen removal mechanism (i.e.Mars-van-Krevelen-type) is excluded, as a rise in the hydrogen signal is also observed (this is not purely stoichiometric because the so-formed H_2 is apparently also re-consumed at these temperatures – see also Panel A). However, the situation is even more complex due to the intermediate appearance of formaldehyde. The latter, as will reported in the MSR section below, appears also as a key intermediate during the methanol steam reforming reaction. Formaldehyde is obviously formed in parallel to CO_2 and decomposes above 580 K, further increasing the hydrogen yield. Putting these results into the perspective of previous results on c-In_2O_3, it turns out the reaction profile of the latter is distinctly different. In that case, c-In_2O_3 does react with CO yielding CO_2, but not via the water-gas shift reaction, but under strict non-catalytic simple and efficient oxygen removal control. The inverse route by replenishing oxygen vacancies by CO_2 is almost entirely blocked.[8] In general, the microkinetics of the water-gas shift equilibrium can follow two distinct pathways, depending on the experimental conditions: a regenerative mechanism involving oxygen vacancies (mostly at high reaction temperatures) and an associative mechanism (usually at low reaction temperatures).[30] The latter involves the adsorption of both CO and H_2O on the oxide surface, the water activation (i.e. heterolytic water splitting into H

and OH) and finally, the reaction to an intermediate, which further reacts towards the products. The core point of the latter mechanism is the nature of the intermediate, which is up to date controversly discussed.[30,31] Formates and/or formic acid intermediates have been reported on different catalysts.[31-36] In the present case, the particular question arises if the observed formaldehyde is formed as a key intermediate *en route* from CO and H_2O to CO_2 and H_2 or if it is an intermediate in a parallel reaction to the actual water-gas shift reaction. Scheme 1 highlights in the involved gas-surface reactions

$$CO + H_2O \leftrightarrows CO_2 + H_2 \quad (1)$$

$$2CO + H_2O \leftrightarrows CO_2 + HCHO \xrightarrow{H_2O} 2H_2 + 2CO_2 \quad (2)$$

Reaction (1) represents the water-gas shift equilibrium, reaction (2) the reaction of CO and H_2O to formaldehyde and its transformation to H_2 and CO_2 with additional water. Reaction (2) is predominantly found at reaction temperatures above ~ 620 K. From the catalytic data it follows that both reactions at least to certain extent are found as parallel reactions, but not as purely sequential reaction steps. This is derived from the parallel onset of both CO_2 and formaldehyde in the initial stages of the reactions and from the sudden break in the hydrogen signal at around 620 K, where formaldehyde reacts further to yield yet another CO_2 and H_2 molecule. While the intermediate to reaction (1) possibly involves influence both from a regenerative and an associative mechanism (due to the strong interaction of CO with rh-In_2O_3 discussed in the preceding section), the intermediate to reaction (2) is to date unknown, but possibly also involves the participation of oxygen vacancies.

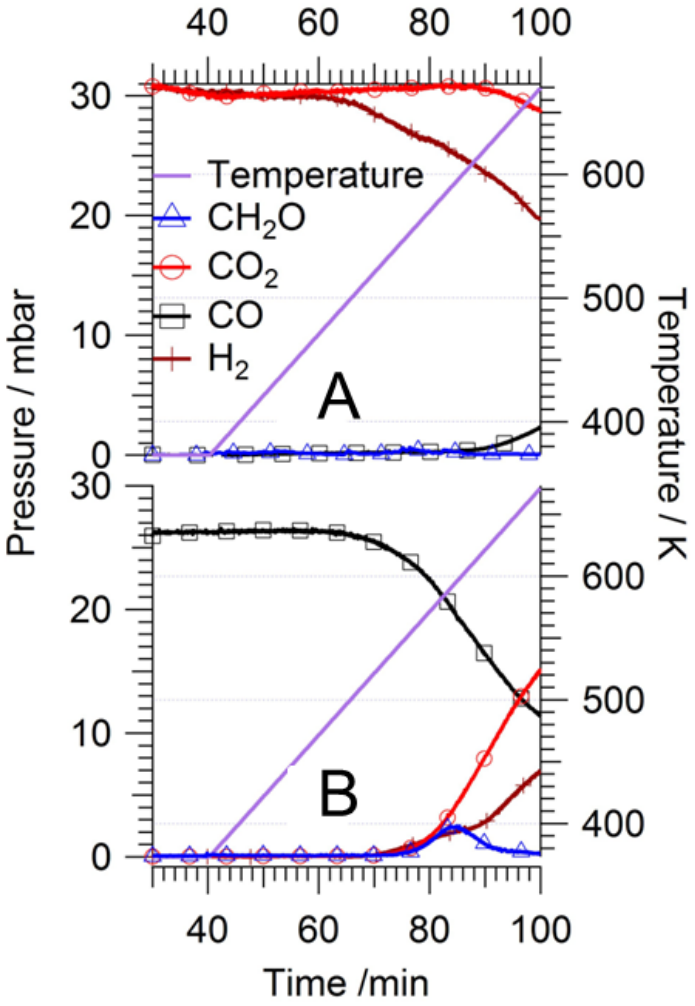

Figure 7: Reaction profile of the (inverse) water-gas shift reaction on rhombohedral In_2O_3. Panel A): inverse water-gas shift reaction, Panel B): water-gas shift reaction. Reaction conditions: 30 mbar CO_2, 30 mbar H_2 for Panel A), 26 mbar CO and 26 mbar H_2O Panel B), 10 mbar argon and He added to 1 bar total pressure. Heating ramp: 10 K min^{-1}. Pre-treatment of the samples include oxidation at 673 K for 1 h in flowing oxygen.

Methanol Steam Reforming

MSR experiments have been conducted on both polymorphic forms under question and are jointly shown in Figure 8. Cubic In_2O_3 (Figure 8 B) shows the anticipated and well-known reaction pattern with very high CO_2-selectivity. No carbon monoxide can be detected and a total methanol conversion of ~ 80 % is obtained at 673 K. In contrast, rh-In_2O_3 shows a distinctly different behavior. Notable methanol conversion starts at around 520 K with a more or less parallel increase of the hydrogen signal. CO_2 is accordingly also formed at roughly similar temperatures. Most notably, CO is only observed at higher temperatures (above ~ 570 K) and formaldehyde species appear as an intermediate species. In line with this observation, only a diminished CO_2 selectivity between 50 and 60%, depending on the reaction degree, is achieved. A closer look at the hydrogen signal reveals a characteristic maximum at 640 K, followed by a drop at 650 K and yet another increase above that temperature. As deduced from the slowing down of the CO_2 trace and from the inverse water-gas shift reaction profiles discussed in detail in Figure 7, this is the temperature where H_2 and CO_2 back-react to CO (and water) via the inverse water-gas shift reaction. The increase of the hydrogen signal at temperatures above 650 K is then due to the decomposition of the intermediarily formed formaldehyde into H_2 and CO. The associated increase in CO is obviously suppressed due to its strong interaction with In_2O_3 (forming e.g. CO_2 via removal of lattice oxygen and the water-gas shift equilibrium), as discussed in the previous section on reducibility. Note that this complex reaction network observed on rh-In_2O_3 is also directly visible in the CO_2 selectivity, finally increasing to its highest value at 673 K (62 %) due to the decomposition of formaldehyde.

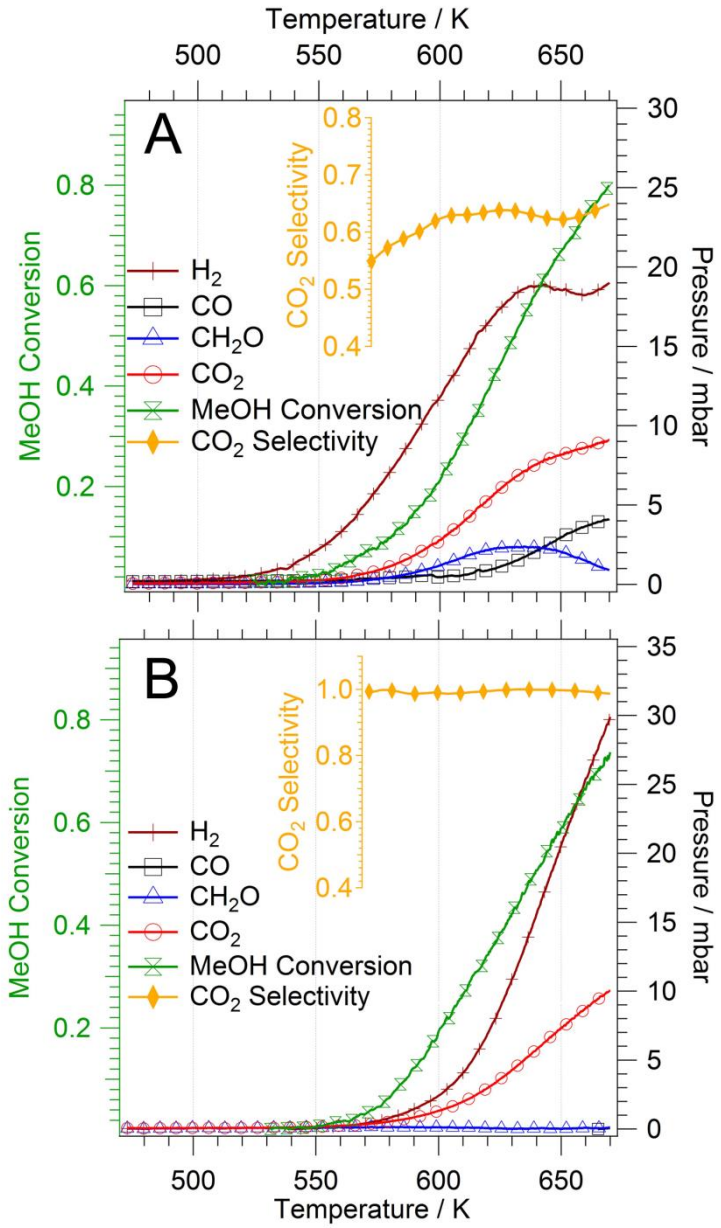

Figure 8: Reaction profiles of the methanol steam reforming reaction on rhombohedral (Panel A) and cubic In_2O_3 (B). Reaction conditions: 15 mbar methanol, 30 mbar water, 10 mbar Ar and He added to 1 bar total pressure. Heating ramp: 10 K min^{-1}. Pre-treatment of the samples include oxidation at 673 K for 1 h in flowing oxygen.

Two important questions remain to be answered at this point: the first one concerns the phase stability during the reaction. As directly revealed in Figure S2, X-ray diffractograms taken after the respective MSR (and (inverse) water-gas shift reaction) runs show that rh-In_2O_3 remains structurally stable and no substantial transformation into c-In_2O_3 takes place.

Secondly, the peculiar MSR reaction pattern of rh-In_2O_3 has to be explained in a comparative view to c-In_2O_3 and, most importantly, also with respect to the (inverse) water-gas shift activity. For the sake of clarity, a brief account of previous findings on c-In_2O_3 should be added at this point.[8,9,27] The latter shows exceptional high CO_2 selectivity in the MSR reaction (close to 99% at 673 K) due its outstanding behavior both in the (inverse) water-gas shift activity and its reactivity towards CO at very low temperatures close to 300 K.[7,8] This reactivity in due course leads to a very efficient transformation of CO into CO_2 via the water-gas shift reaction, but at the same time, the backward reaction from CO_2 and H_2 to CO (and water) is effectively blocked. This behavior has been explained by the water-gas shift reaction predominantly following a vacancy-mediated mechanism and a very high activation barrier for the replenishment of the so-induced oxygen vacancies by CO_2 (via the inverse reaction).[8] This behavior (and the associated high CO_2 selectivity in MSR) is typical for oxides with predominant basic surface sites (like c-In_2O_3), enabling both efficient H abstraction from the adsorbed methanol and a very fast onward reaction of the intermediate formaldehyde species to CO_2.[37] Therefore, on c-In_2O_3 no formaldehyde is observed as gas-phase intermediate and in fact, dedicated formaldehyde steam reforming reactions revealed similarly high CO_2 selectivities comparable to those observed via MSR.[8] In contrast, oxides with a corresponding higher number of acidic surface sites (like rh-In_2O_3) tend to form more intermediate oxygenates (such as formic acid-related intermediates) and condensed molecules (such as dimethylether).[37] A instructive example in this respect is the Ga_2O_3 polymorphic system: on the β-Ga_2O_3 modification, due its high number of acidic surface sites, formic acid could be detected as intermediate. The more basic α-Ga_2O_3 polymorph in contrast showed CO_2 selectivities up to 70 %.[38] From this discussion, we directly infer a corresponding less-pronounced basic character of the surface sites on rh-In_2O_3, in contrast to c-In_2O_3, but at the same time also without a pronounced acidic character, as no formic acid or condensed intermediates are in parallel observed. Most interesting, rh-In_2O_3 seems to exhibit special

adsorption sites stabilizing formaldehyde obviously long enough to detect it as gas-phase intermediate, before final decomposition into H_2 and CO takes place.

The difference in the reactivities is also reflected upon consideration of the CO_2-related turnover frequency numbers (TOF's) and the calculation of the apparent activation energies. The estimation is based on the sample mass (70 mg rh-In_2O_3, 60 mg c-In_2O_3), the densities of the oxide structures, their molar mass (277.6 g mol^{-1}) and their specific surface areas (43.5 m^2 g^{-1} for rh-In_2O_3, 0.74 m^2 g^{-1} for c-In_2O_3) as well as the definition of one In-O entity as catalytic active site. This yields $3.80x10^{19}$ In-O sites for rh-In_2O_3 and $5.54x10^{17}$ sites for c-In_2O_3. Based on these numbers, the TOF's can be estimated and are summarized in Table 3.

Table 3: Overview of the CO_2-related catalytic turnover frequency numbers in methanol steam reforming, as obtained on rh- and c-In_2O_3.

Sample	CO_2 TOF/ s^{-1} In-O site^{-1}	CO_2 TOF/ h^{-1} In-O site^{-1}
rh-In_2O_3		
593 K	$6.68x10^{-5}$	0.24
613 K	$1.05x10^{-4}$	0.38
623 K	$9.68x10^{-5}$	0.35
653 K	$3.26x10^{-5}$	0.12
c-In_2O_3		
593 K	$2.18x10^{-3}$	7.8
623 K	$6.25x10^{-3}$	22.5
643 K	$7.73x10^{-3}$	27.8
653 K	$7.34x10^{-3}$	26.4

As can be clearly seen, the maximum turnover frequency obtained at the highest reaction temperatures on c-In_2O_3 exceeds that of rh-In_2O_3 by a factor of 200, although the methanol conversion is almost equal at about 80 %. The higher reactivity is also derived from the lower apparent energy of 121 kJ mol^{-1} for c-In_2O_3, in comparison to 137 kJ mol^{-1} for rh-In_2O_3, as derived from an Arrhenius analysis of the initial reaction rates.

As a concluding remark, we note that the X-ray diffractograms (shown in Figure S2) reveal that none of the treatments reported in this section causes substantial transformation of rh- into c-In_2O_3, an obvious pre-requisite for catalytic characterization.

4. Conclusions

In conclusion, we were successful in providing an in-depth physico-chemical and catalytic characterization of the corundum-type rhombohedral-type In_2O_3 phase. In due course, gas-phase dependent stability limits with respect to the transformation to the cubic polymorphs as well as to metallic In after reduction in hydrogen and carbon monoxide were established. Summarizing, treatment in either of the reduction agents caused distinctly different changes in the crystal structure of initial rh-In_2O_3 and thereby, the relative amounts of still persisiting rh-In_2O_3 and newly formed cubic In_2O_3 and metallic In. As for behavior in the (inverse) water-gas shift reaction and methanol steam reforming, rh-In_2O_3 behaves distinctly different from its cubic counterpart, as it effectively catalyses the inverse water-gas shift reaction route. As a consequence, the CO_2 selectivity in methanol steam reforming is at ~60% much lower than observed on cubic In_2O_3. On the latter, the inverse water-gas shift route is almost entirely blocked, giving rise to almost 100% CO_2 selectivity in methanol steam reforming. This obviously is due to the different reactivity of the lattice oxygen in both In_2O_3 modifications and the associated reactivity of the reduction-created oxygen vacancies. As an obvious prerequisite to monitor the catalytic behavior of rh-In_2O_3, the latter proved especially stable in water-gas shift and methanol steam refoming mixtures. Finally, we deem the studies a first step to a better understanding of the chemistry of the In-O system and its various modifications, and anticipate that the ideas can be directly transferred to other even less-common In_2O_3 polymorphs.

5. Acknowledgements

We thank the FWF (Austrian Science Foundation) for financial support under the project FOXSI F4503-N16. The work has been performed within the framework of the platform "Materials and Nanoscience at the University of Innsbruck. Acknowledgement goes also to the DFG under project „Kristalline Nichtgleichgewichtsphasen - Präparation, Charakterisierung und in situ-Untersuchung der Bildungsmechanismen" (SPP 1415), grant GU 992/12-1.

Supporting Information Available

Structure models; Additional X-ray diffractograms

References

[1] Bekheet M. E.; Schwarz M. R.; Lauterbach S.; Kleebe H. J.; Knoll P.; Riedel R.; Gurlo A.; Orthorhombic In_2O_3: A Metastable Polymorph of Indium Sesquioxide. *Angew. Chemie Intl. Ed.* **2013**, *52*, 6531-6535

[2] Lee C. H.; Kim M.; Kim T.; Kim A.; Paek J.; Lee J.; Choi S.; Kim K.; Park J.; Lee K., Ambient Pressure Synthesis of Size-Controlled Corundum-Type In_2O_3 Nanocubes. *J. Amer. Chem. Soc.* **2006**, *128*, 9326-9327

[3] Gurlo A., Structural Stability of High-Pressure Polymorphs in In_2O_3 Nanocrystals: Evidence of Stress-Induced Transition. *Angew. Chemie Intl. Ed*. **2010**, *49*, 5610-5612

[4] Garcia-Domene B. et al. Pbca-Type In_2O_3: The High-Pressure Post-Corundum Phase at Room Temperature, *J. Phys. Chem. C* **2014**, *118*, 20545-20552

[5] Sood S.; Gouma P., Polymorphism in Nanocrystalline Binary Metal Oxides. *NanoMat Energ.* **2013**, *2*, 82-96

[6] Gurlo A., Nanosensors: Towards Morphological Control of Gas Sensing Activity. SnO_2, In_2O_3, ZnO and WO_3 Case Studies. *Nanoscale* **2011**, *3*, 154-165

[7] Bielz T.; Lorenz H.; Amann P.; Klötzer B.; Penner S., Water-Gas Shift and Formaldehyde Reforming Activity Determined by Defect Chemistry of Polycrystalline In_2O_3, *J. Phys. Chem. C* **2011**, *115*, 6622-6628

[8] Lorenz H.; Stöger-Pollach M.; Schwarz S.; Pfaller K.; Klötzer B.; Penner S., Novel Methanol Steam Reforming Activity and Selectivity of Pure In_2O_3. *Appl. Catal. A* **2008**, *347*, 34-42

[9] Kominami, H.; Nakamura, T.; Sowa, K.; Nakanishi, Y.; Hatanaka, T.; Shimaoka, G. Low Voltage Cathodoluminescent Properties of Phosphors Coated with In_2O_3 by Sol-Gel Method. *Appl. Surf. Sci.* **1997**, *113-114*, 519-522

[10] Ivanovskaya, M., Gurlo, A.; Bogdanov, P. Mechanism of O_3 and NO_2 Detection and Selectivity of In_2O_3 Sensors. *Sens. Actuat. B* **2001**, *77*, 264-267

[11] Sanders, D.; Simon, U. High-Throughput Gas Sensing Screening of Surface-Doped In_2O_3. *J. Comb. Chem.* **2007**, *9*, 53-61

[12] Umegaki, T., Kuratani, K.; Yamada, Y.; Ueda, A.; Kuriyama, N.; Kobayashi, T.; Xu, Q. Hydrogen Production via Steam Reforming of Ethyl Alcohol over Nano-Structured Indium Oxide Catalysts. *J. Power Sources* **2008**, *179*, 566-570

[13] Gervasini, A.; Perdigon-Melon, J. A.; Guimon, C.; Auroux, A. An In-Depth Study of Supported In_2O_3 Oxide as a Potential Environmental Catalyst: The Influence of the Oxide Support. *J. Phys. Chem B* **2006**, *110*, 240-249

[14] Zhang, D. H.; Li, C.; Han, S.; Liu, X. L.; Tang, T.; Jin, W.; Zhou, C. W. Electronic Transport Studies of Single-Crystalline In_2O_3 Nanowires. *Appl. Phys. Lett.* **2003**, *82*, 112-114

[15] (a) Otsuka, K.; Yasui, T.; Morikawa, A. The Decomposition of Water on the CO- or H_2-Reduced Indium Oxide. *Bull. Chem. Soc. Jpn.* **1982**, *55*, 1768-1771,

[16] Yin, J.; Cao, H. Synthesis and Photocatalytic Activity of Single-Crystalline Hollow rh-In_2O_3 Nanocrystals. *Inorg. Chem.* **2012**, *51*, 6529-6536 and references therein

[17] Gurlo, A.; Lauterbach, S.; Miehe, G.; Kleebe, H.; L. Riedel, R. Nanocubes or Nanorhombohedra? Unusual Crystal Shapes of Corundum-Type Indium Oxide. *J. Phys. Chem.* C **2008**, *112* 9209-9213

[18] Bekheet, M. F.; Schwarz, M. R.; Kroll, P.; et al. Kinetic Control in the Synthesis of Metastable Polymorphs: Bixbyite-to-Rh_2O_3(II)-to-Corundum Transition in In_2O_3. *J. Solid State Chem.* **2015**, *229*, 278-286

[19] Bekheet, M. F.; Schwarz, Marcus R.; Lauterbach, Stefan; et al. In situ High Pressure High Temperature Experiments in Multi-Anvil Assemblies with Bixbyite-Type In_2O_3 and Synthesis of Corundum-Type and Orthorhombic In_2O_3 Polymorphs, *High Press. Res*. **2013**, *13*, 697-711

[20] Gurlo, A.; Dzivenko, D.; Kroll, P.; et al.High-Pressure High-Temperature Synthesis of Rh_2O_3-II-type In_2O_3 Polymorph, *Phys. Stat. Sol. Rap. Res. Lett.* **2008**, *2*, 269-271

[21] Yusa, H.; Tsuchiya, T.; Sata, N.; Ohishi, Y. Rh_2O_3(II)-type Structures in Ga_2O_3 and In_2O_3 Under High Pressure: Experiment and Theory. *Phys. Rev. B*, **2008**, *77*, 064107-064113.

[22] Yusa, H., Tsuchiya, T.; Tsuchiya, J.; Sata, N.; Ohishi, α-Gd_2S_3-type Structure in In_2O_3: Experiments and Theoretical Confirmation of a High-Pressure Polymorph in Sesquioxide. *Phys. Rev. B*, **2008**, *78*, 092107-092112.

[23] Dong, H.; Chen, Z.; Sun, L.; Zhou, L.; Ling, Y.; Yu, C.; Tan, H.; Jagadish, C.; Shen, X. Nanosheets-Based Rhombohedral In_2O_3 3D Hierarchical Microspheres: Synthesis, Growth Mechanism, and Optical Properties, *J. Phys. Chem. C* **2009**, *113*, 10511-10516

[24] Schlicker, L.; Bekheet, M.; Gurlo, A. Scaled-up Synthesis of Metastable Indium Oxyhydroxide (InOOH) and Corundum-Type rh-In_2O_3, *Zeitschrift für Kristallographie - Crystalline Materials*, submitted.

[25] King, P. D.C. Band Gap, Electronic Structure and Surface Electron Accumulation of Cubic and Rhombohedral In_2O_3. *Phys. Rev. B* **2009**, *79*, 20511-20518

[26] de Boer, T.; Bekheet, M. F.; Gurlo, A.; Riedel, R.; Moewes, A. Band Gap and Electronic Structure of Cubic, Rhombohedral, and Orthorhombic In_2O_3 Polymorphs: Experiment and Theory. *Phys. Rev. B* **2016**, *93*, 155205

[27] Bielz, T.; Lorenz, H.; Jochum, W.; Kaindl, R.; Klauser, F.; Klötzer, B.; Penner, S. Hydrogen on In_2O_3: Reducibility, Bonding, Defect Formation and Reactivity, *J. Phys. Chem. C* **2010**, *114*, 9022-9028

[28] Thalinger, R.; Opitz, A. K.; Kogler, S.; Heggen, M.; Stroppa, D.; Schmidmair, D.; Tappert, R.; Fleig, J.; Klötzer, B.; Penner, S. Water-Gas Shift and Methane Reactivity on Reducible Perovskite-Type Oxides. *J. Phys. Chem. C* **2015**, *23*, 2-14

[29] Köck, E. M.; Kogler, M.; Pramsoler, R.; Klötzer, B.; Penner, S. A High-Temperature, Ambient-Pressure Ultra-Dry In-Operando Reactor Cell for FT-IR Spectroscopy. *Rev. Sci. Instr*. **2014**, *85*, 084102-1 – 084102-8

[30] Byron Smith, R. J.; Loganathan, M.; Shanta, M. S. A Review of the Water-Gas Shift Reaction Kinetics, *Int. J. Chem. React. Eng.* **2010**, *8*, 1-32

[31] Rhodes, C.; Hutchings, G.J.; Ward, A.M. WGSR: Finding the Mechanistic Boundary. *Catal. Today* **1995**, *23*, 43 – 58

[32] Grenoble D. C.; Estadt, M. M. The Chemistry and Catalysis of the Water Gas Shift Reaction 1 The Kinetics over Supported Metal Catalysts. *J. Catal.* **1981**, *67*, 90-102

[33] Ovesen, C. V.; Stoltze, P.; Norskov J. K.; Campbell, C. T. A Kinetic Model of the Water Gas Shift Reaction. *J. Catal.* **1992**, *134*, 445-468

[34] Ovesen, C. V.; Clausen, B. S.; Hammershøi, B. S.; Steffensen, G.; Askgaard, T.; Chorkendorff, I.; Nørskov, J. K.; Rasmussen, P. B.; Stoltze, P.; Taylor, P. A Microkinetic Analysis of the Water–Gas Shift Reaction under Industrial Conditions. *J. Catal.* **1996**, *158*, 170–180

[35] Gideon Botes, F. Water–Gas-Shift Kinetics in the Iron-Based Low-Temperature Fischer–Tropsch Synthesis. *Appl. Catal. A* **2007**, *328*, 237–242

[36] Sun, J.; DesJardins, J.; Buglass, J.; Liu, K. Noble Metal Water Gas Shift Catalysis: Kinetics Study and Reactor Design. *Intl. J. Hydr. Energ*. **2005**, *30*, 1259-1264

[37] Tatibouet, J.M. Methanol Synthesis As A Catalyst Surface Probe. *Appl. Catal. A* **1997**, *148*, 213-252

[38] Lorenz, H.; Thalinger, R.; Köck, E.-M.; Kogler, M.; Mayr, L.; Schmidmair, D.; Bielz, T.; Pfaller, K.; Klötzer, B.; Penner, S. Methanol Steam Reforming: CO_2-selective Pd_2Ga Phases Supported on α- and γ-Ga_2O_3. *Appl. Catal. A* **2013**, *453*, 34-44

TOC Graphic

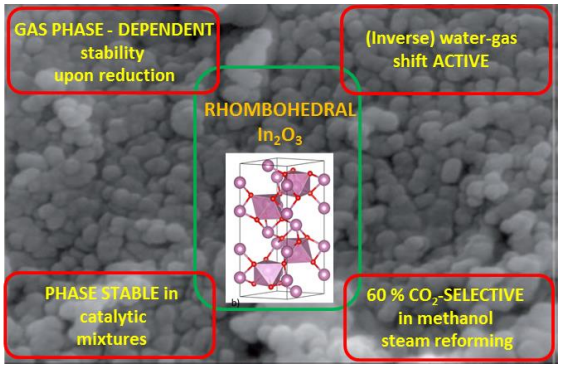
GAS PHASE - DEPENDENT stability upon reduction
(Inverse) water-gas shift ACTIVE
RHOMBOHEDRAL In_2O_3
PHASE STABLE in catalytic mixtures
60 % CO_2-SELECTIVE in methanol steam reforming